AIAA JOURNAL
Vol. 46, No. 10, October 2008

Development of a Preliminary Model-Scale Adaptive Jet Engine Chevron

Travis L. Turner,* Randolph H. Cabell, Roberto J. Cano, and Richard J. Silcox
NASA Langley Research Center, Hampton, Virginia 23681-2199

DOI: 10.2514/1.35939

Reduction of jet noise continues to be an important research topic. Exhaust-nozzle chevrons have been shown to reduce jet noise, but parametric effects, including immersion amount and azimuthal distribution, are not well understood. Additionally, thrust loss due to static chevrons at cruise suggests a significant benefit from deployable chevrons. The focus of this study is the development of an adaptive-chevron concept for the primary purpose of parametric studies for jet noise reduction in the laboratory and secondarily for development of technology that can be leveraged for full-scale systems. The adaptive-chevron concept employed in this work consists of a laminated composite structure with embedded shape memory alloy actuators. The actuators are embedded on one side of the middle surface such that joule heating of the actuators causes them to attempt recovery of prestrain, thereby generating a moment and deflecting the structure. A brief description of the chevron design is given followed by details of the fabrication approach. Results from bench-top tests are presented and correlated with numerical predictions from a model for such structures that was previously implemented in MSC.Nastran and ABAQUS. Excellent performance and agreement with predictions is demonstrated. Results from tests in a representative flow environment are also presented. Excellent performance is again achieved for both open- and closed-loop tests, the latter demonstrating control of deflection to a specified immersion into the flow. The actuation authority and immersion performance is shown to be relatively insensitive to nozzle pressure ratio. Very repeatable immersion control with modest power requirements is demonstrated.

Nomenclature

A = austenitic transformation temperature
E = Young's modulus
G = shear modulus
M = martensitic transformation temperature or Mach number
P = pressure
T = temperature
v = volume fraction
V = velocity
α = coefficient of thermal expansion
ε = normal strain
ν = Poisson's ratio
σ = normal stress

Subscripts

a = actuator (shape memory alloy)
aw = adiabatic wall
f = finish
ideal = ideal gas
m = matrix material
r = recovery stress (shape memory alloy)
s = start
t = total
1 = orthotropic principal material coordinate 1
2 = orthotropic principal material coordinate 2
12 = 1–2 plane of an orthotropic material

I. Introduction

REDUCTION of jet engine noise in the vicinity of airports continues to be of paramount importance. Jet exhaust-nozzle *chevron* systems are a proven noise-reduction technology [1], but much is yet to be learned about their parametric design space, and a tradeoff between noise reduction at takeoff and thrust loss at cruise has slowed their incorporation into production engines. Chevrons produce a scalloped or serrated trailing edge to a jet exhaust nozzle and protrude into the exhaust flow. All model-scale noise reduction and/or flow studies involving chevrons have been performed using static chevron technology, in which the geometry and resulting flow immersion are predetermined and invariant [2–15]. These studies typically included some parametric investigation of chevron number, geometry, and/or immersion. However, detailed parametric investigations using static chevrons have not been conducted because of the high cost of fabricating and testing separate nozzle systems. Computational studies are also limited in their ability to investigate the parametric design space because current numerical tools lack the aeroacoustic fidelity needed for design.

One means of simultaneously addressing immersion parametric design (i.e., immersion amount and azimuthal distribution) and the tradeoff of noise reduction and thrust penalty is the development of adaptive (deployable) chevrons. The adaptive-chevron application appears to be ideal for shape memory alloy (SMA) actuation technology because SMA actuators can be thermally activated, they produce large force and stroke, and the quasi-static nature of adaptive-chevron requirements alleviates issues associated with the limited frequency response of the thermoelastic shape memory effect. Shape memory alloys exhibit a phase transformation that is driven by temperature and stress. The thermally induced phase transformation is responsible for the well-known shape memory effect (SME) that is of primary interest in this study. Shape memory alloys can recover a large strain by the SME when heated in an unconstrained configuration and generate large forces when strain recovery is prevented. Thus, the general concept for a SMA-enabled adaptive chevron entails deploying the chevron under the actuation authority of prestrained SMA actuators.

SMA actuators can be employed in various ways to enable adaptive chevrons. Research has appeared in the literature that is related to this goal. Bruck et al. [16] developed a beam-bending

---

Received 30 November 2007; revision received 22 April 2008; accepted for publication 7 May 2008.

*Structural Acoustics Branch, Building 1208, Room 110, Mail Stop 463; t.l.turner@nasa.gov (Corresponding Author).

concept involving polyurethane matrix materials with embedded and opposing one-way-trained SMA actuators. Their work showed that at least 25% greater recovery strains can be achieved via opposing one-way actuation than with two-way actuation. They also found that inducing bending deformation by in-plane actuation was compromised by excessive compliance in the matrix material of the parent structure. Kim et al. [17] investigated the effects of elastic tailoring (e.g., composite ply angles) on bend and twist deformations of composite beams. The results of this numerical study indicate that large and complex bending shape changes can be achieved by exploiting coupling (i.e., bend extension and bend twist) stiffness of composite laminates. Chandra [18] reported results of SMA bender elements embedded in composite beams for delivering bend and twist authority by exploiting bend-twist coupling of the composite layup. Baz et al. [19] also incorporated bender elements within sleeves on the neutral axis of composite beams to control bending deflections without incurring the effects of in-plane stress.

The only SMA-enabled adaptive-chevron concept known from the literature, other than the work of the present authors, was reported in [20–22]. The adaptive-chevron concept described in those references involves the use of nitinol bender elements that are fastened to and work against a metallic or composite main structure to provide deflection control. Previous work has demonstrated various structural control concepts via SMA hybrid composite (SMAHC) laminates [23–25]. In all cases, prestrained (elongated) nitinol actuators were embedded in a composite during lamination and restrained during elevated temperature cure. Joule heating of the actuators in these structures produced stiffness changes for thermoelastic and vibroacoustic control. This previous work was leveraged for the adaptive-chevron concept considered in this study, which consists of nitinol actuators embedded on one side of the neutral axis of a laminated composite. Thus, thermal excitation causes the actuators to attempt recovery of the prestrain under the constraint of the bond to the host material. The resulting asymmetry in thermal stress causes a moment that deflects the structure out of plane to the immersed configuration. The force developed in the host composite due to elastic strain during deflection and the aerodynamic load due to engine flow are used to restore the structure to the retracted position.

Previous work by Turner et al. [26] demonstrated the feasibility of the adaptive SMAHC chevron concept. That study also provided the first shape-control experimental validation of a commercially available (MSC.Nastran and ABAQUS) constitutive model for SMAHC materials and structures [27–29]. However, the deflection performance of that SMAHC chevron design fell short of the requirement, and shortcomings in the fabrication approach were identified. The objectives of the present study are to design (via the validated numerical tool) a SMAHC chevron that meets the performance requirements, develop a refined fabrication approach to increase predictability and repeatability, perform bench-top testing of the refined chevron prototype, and test the performance of the SMAHC chevron prototype in flow conditions representative of the jet engine environment. The longer-term objective of the project, for which this study forms a part, is to enable parametric studies in the laboratory to investigate effects such as variable immersion depth and azimuthal distribution for optimal jet noise reduction. Thus, the present study focuses on chevron systems at model scale, and provisions are made to electrically activate the SMA actuators to enable adaptive control.

II. SMAHC Chevron Fabrication

A picture of static chevrons on the core and bypass nozzles of a model installed on the jet engine simulator in the NASA Langley Research Center (LaRC) Low-Speed Aeroacoustic Wind Tunnel is shown in Fig. 1. The model was approximately 1:9 scale of a bypass-ratio-5 engine with core and bypass-nozzle diameters of 12.807 and 23.922 cm, respectively. The corresponding core and bypass-nozzle areas were 72.96 and 186.62 cm^2, respectively. The engine model incorporated a pylon and had chevron planform dimensions of approximately 2.5 × 4.8 cm. The chevron thickness was constant at 0.064 cm and the static immersion of each chevron tip was 0.127 cm without flow loading effects. The geometry and static immersion of this chevron system was specified as the result of previous numerical and experimental studies. The present effort is focused on developing adaptive-chevron technology for the bypass nozzle of a similar engine model by detailed study of individual chevrons. This concept cannot be extended to the core engine nozzle at the present time because of temperature limitations of commercial SMA materials ($A_s \leq 110°\mathrm{C}$ for nitinol). The focus of this study is further restricted to flat chevrons (i.e., without the cylindrical radius of curvature), for simplicity in developing a viable concept.

Previous work presented a fabrication approach, test results, and validation of a numerical model for a SMAHC chevron concept with a single embedded actuator assembly [26]. It was found that the single-actuator assembly provided insufficient actuation authority and limitations of the fabrication approach dictated development of a new procedure for embedding multiple actuators. Numerical analyses subsequent to the previous study indicated that a dual-actuator-assembly configuration was sufficient to achieve the chevron tip deflection goal of 0.127 cm. The requirements for electrical activation of the SMA actuators and for a clean trailing edge mandated electrical continuity of the actuator(s) within the chevron and actuator ingress/egress points at the chevron root. These constraints were accommodated in the fabrication approach by incorporating joints between two layers of nitinol within the laminate to provide for electrical continuity. A schematic of the SMAHC chevron concept with dual-actuator assemblies incorporating this internal joint is shown in Fig. 2. The section schematic illustrates the asymmetric actuator placement in the thickness direction to induce bending.

The general fabrication process that was employed in the present study consists of lamination of oversized prepreg layers, consolidation by vacuum hot-press cure, and machining to final dimensions. Lamination of oversize layers was performed, in lieu of

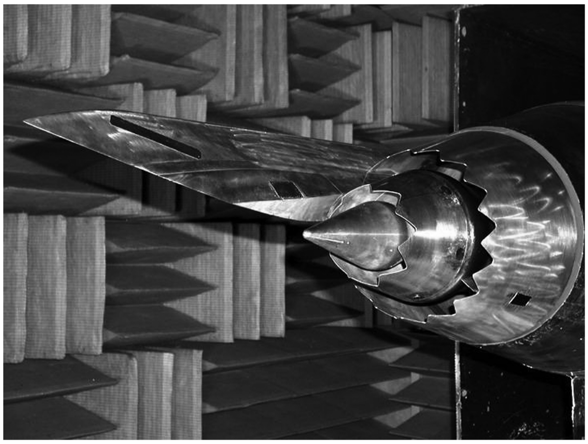

Fig. 1 Static chevron scale-model nozzle.

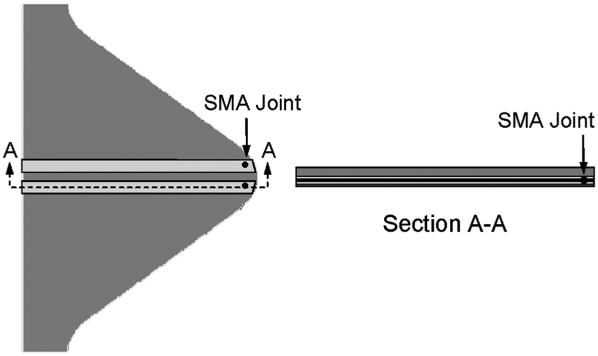

Fig. 2 Schematic of the SMAHC chevron concept.

die-cut net-shaped layers, to take advantage of existing molds and to allow for the most flexibility in planform geometry and layup/cure tooling. Details of the fabrication process are clearer in the following description of a representative fabrication sequence.

A SMAHC material system consisting of glass-epoxy unidirectional preimpregnated (prepreg) tape and nitinol ribbon was selected for the present study. This material combination was selected because of several favorable properties and familiarity from previous experience. The glass-epoxy matrix material offers electrical isolation for resistive heating of the SMA actuators and affords visual flaw detection. Prepreg material is available in thin layers and allows precise control over directional stiffness. The glass-epoxy material is an S2-glass/3501-6 resin material system with a nominal cured ply thickness of 0.01 cm. A nitinol alloy was selected due to its electrical resistance, shape memory capability, and availability. The ribbon (rectangular cross-sectional wire) configuration simplified the fabrication procedure, by minimizing the number of actuators, and the mechanical/electrical connectivity of the structure in service. The nitinol ribbon had a weight-percent composition of 55.4Ni-44.3Ti-0.3X, where X indicates impurity content, and was obtained with nominal cross-sectional dimensions of 0.229×0.015 cm. The unconstrained transformation temperatures were determined by differential scanning calorimetry (DSC) to be $A_s = 45^\circ\mathrm{C}$, $A_f = 60^\circ\mathrm{C}$, $M_s = 17^\circ\mathrm{C}$, and $M_f = 0^\circ\mathrm{C}$.

The nitinol ribbon material was prestrained (elongated) 4% and lightly sandblasted to remove the oxide layer for improved nitinol–nitinol joining and nitinol–resin adhesion purposes. Pairs of the nitinol ribbon were aligned and spot-welded in an argon atmosphere at a location along the length of the actuators convenient for placement at the intended chevron tip during the lamination process. The joint actually consisted of three consecutive welds approximately 0.127 cm apart and spanning approximately 0.254 cm of the actuator-assembly length. A representative spot-welding process was observed with an infrared camera and it was found that the thermal pulse traveling away from the weld site had a maximum temperature of approximately 32°C closest to the weld and dissipated completely at a distance of less than 0.953 cm from the weld site. Thus, it is anticipated that the spot-welding process had minimal effect on the nitinol actuators, except in the immediate vicinity of the welds.

It was previously determined that material dimensions and chevron design constraints required the use of at least five plies of glass epoxy. Plies of the glass-epoxy material were cut to fit an existing 5.08×5.08 cm vacuum hot-press mold and lamination was performed according to the following sequence: $-45/+45/90/\mathrm{SMA}/+45/\mathrm{SMA}/-45$. The upper +45-deg layer was cut into 3.56- and 1.52-cm segments, and the 1.52-cm segment was added to the $-45/+45/90$ layup at the outboard edge before installing the actuator assemblies. The actuator assemblies were positioned symmetrically about the layup centerline with an outside-to-outside edge dimension of 0.63 cm. Additionally, the actuators were positioned with the spot welds resting on the 1.52-cm +45-deg segment with the innermost weld adjacent to the inner edge of the segment, as shown in Fig. 3. The 3.56-cm +45-deg segment was inserted between the two strands of nitinol in each actuator assembly and worked as close to the first weld as possible, thereby making a close fit with the 1.52-cm, +45-deg segment. The final −45-deg ply was added to the layup, and the assembly was installed in the mold with an orientation that placed the intended root edge of the chevron against a resin dam, as shown in Fig. 4. The large mold depth is an artifact of its previous use and is not necessary for the present fabrication process. Note that a layer of polyimide release film and bleeder cloth was placed beneath and on top of the laminate during insertion in the mold. The nitinol actuators protruded through a slit in the resin dam on the chevron root side of the mold and directly from the mold mating surfaces on the opposite side. Gripping assemblies rigidly restrained the nitinol on both sides of the mold.

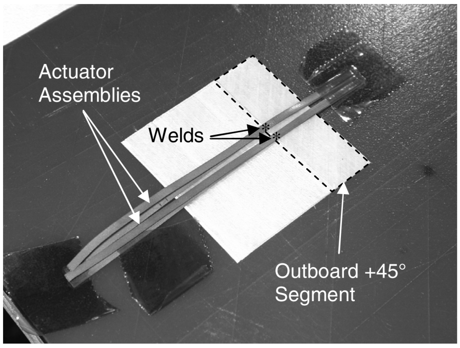

Fig. 3 Actuator assemblies placed on the layup.

The laminate was subjected to the cure cycle recommended by the prepreg manufacturer, heated from room temperature to 121°C at 2–3°C/ min, held for 15 min at 121°C, 586 kPa of pressure was applied, held at 121°C and 586 kPa for an additional 45 min, heated again to 177°C at 2–3°C/ min while holding 586 kPa, held at 177°C and 586 kPa for 2 h, cooled to room temperature at 2–3°C/ min while holding 586 kPa, and the pressure was released at room temperature. The resulting consolidated laminate is shown in Fig. 5. The resin dam provided a reference edge for machining the laminate to final chevron dimensions, the result of which is shown in Fig. 6. The nitinol leads remaining at the root edge of the chevron were

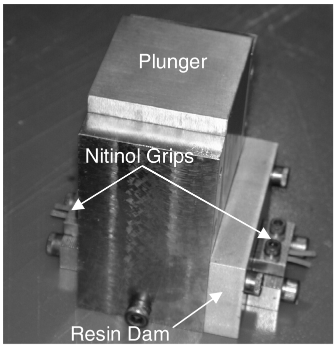

Fig. 4 Finished layup installed in mold.

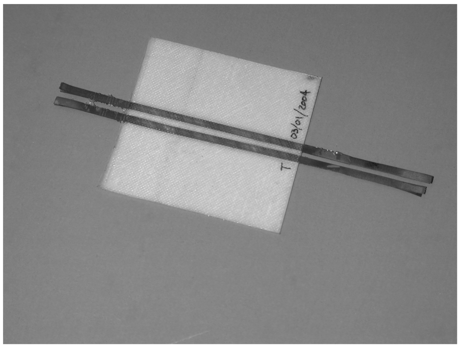

Fig. 5 Consolidated SMAHC laminate.

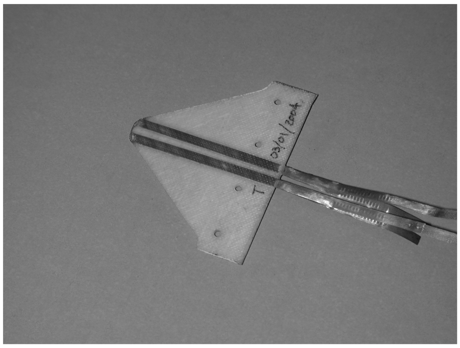

Fig. 6 SMAHC chevron.

copper-plated to enable soldering to the leads and to improve contact-type electrical connections.

Although the laminate was asymmetric due to the embedded nitinol ribbon, no warping of the laminate resulted after cure because the restraint on the actuators prevented recovery of the prestrain and participation in generation of a thermal moment during cooling. The consolidated laminate had a thickness of approximately 0.064 cm in the region away from the nitinol and 0.071 cm in the region with the nitinol. It is apparent that there was significant compaction of the glass epoxy in the vicinity of the nitinol due to the vacuum hot-press consolidation approach. Conversely, the region away from the nitinol exhibited a thickness greater than the nominal thickness indicated by the vendor. The measured thicknesses and other attributes from multiple chevrons showed a high degree of dimensional repeatability.

III. Bench-Top Testing

A chevron fabricated by the process described in the previous section was tested on the bench top to determine baseline performance, to provide experimental data under a tightly controlled environment for further numerical model validation, and to thermally cycle the chevron to render it thermomechanically stable.

A. Experimental Arrangement

The test system, shown in Fig. 7, consisted of an optical bench for accurate component placement, a digital infrared (IR) camera for full-field temperature measurement, a projection Moiré interferometry (PMI) system for full-field out-of-plane displacement measurement, a laser displacement transducer (LDT) for single-point displacement measurement, and a test control and data acquisition system. The LDT had a measurement range of 3 cm and a resolution of 3 μm. The IR and PMI cameras were positioned approximately 76 cm from the chevron. The IR camera had a 32.394 × 24.138 cm field of view (width and height) and a spatial resolution of 0.101 cm. The IR camera was used on a 0–500°C range, resulting in a temperature resolution of 0.03°C. The IR measurements were calibrated by setting the target emissivity to the total hemispherical emissivity of the chevron, which had been measured previously. The PMI video camera had a field of view of 7.303 × 5.715 cm with a spatial resolution of 5.39e–3 cm and the video was digitized to 8 bits. The PMI system projector was used to project a series of equispaced parallel lines with a nominal pitch of 0.066 cm onto the chevron surface. The PMI system was calibrated over a range that exceeded the anticipated range of chevron deformation and achieved a nominal random measurement error of ±0.0030 cm. The LDT was positioned on the side opposite the IR and PMI cameras and normal to the chevron surface near the tip.

A close-up view of the chevron mounted to the support post is shown in Fig. 8. The side of the chevron facing the IR and PMI systems was painted white to provide an opaque and diffuse scattering surface for the PMI system, which resulted in a total hemispherical emissivity of 0.9 for calibration of the IR data. The chevron was configured such that the actuators were closest to the painted surface of the chevron and the chevron was bent toward the IR and PMI cameras upon actuation. The chevron was fastened to the post, and mechanical and electrical connections to the nitinol actuator assemblies were made in the grip assembly attached at the back of the mounting post. The grip assembly consisted of electrically separated copper-plated contacts embedded in a carrier, made from fiberglass board material, and a clamping bar with copper plating on the grip face, as shown in the inset of Fig. 8. The fiberglass carrier electrically isolated the grip assembly from the support post. A layer of polyimide tape insulated the two nitinol leads of each actuator assembly from one another, starting at the edge of the chevron and ending at the back edge of the clamping bar (not shown in Fig. 8). Thus, an electrical power connection was made to the bottom lead of each actuator assembly, indicated by ± in Fig. 8, and continuity was provided by the spot welds within the chevron and by the copper-plated clamping bar in the grip assembly. All of the nitinol ribbon was configured electrically in series in this manner.

The LDT laser spot was positioned at a point on the chevron centerline and approximately 0.127 cm from the tip. This location is indicated on the opposite side of the chevron in Fig. 8 by the red asterisk. Regions of interest (ROI) including a rectangle encompassing the entire chevron, and two lines along the centerline of each nitinol actuator assembly, from the tip of the chevron to the edge of the support post, were defined in the data acquisition and control system, as shown schematically in Fig. 8. Thermal cycles were performed on the chevron by prescribing a set-point distribution for the average temperature of the top line ROI consisting of 5.6°C increments from room temperature to 121°C and back to room temperature. Feedback control was achieved via a proportional–integral-type controller using this average temperature as the control metric. Power was supplied to the chevron by a dc power supply operated in constant current mode and controlled by analog voltage. IR data were collected continuously for control purposes, but were only recorded at the set points. The analog voltage and PMI data were also recorded at the set points. The PMI system acquired 10 images and averaged them at each set point for offline processing.

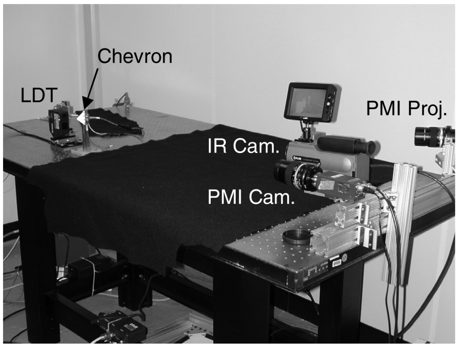

Fig. 7 Overview of the chevron test system.

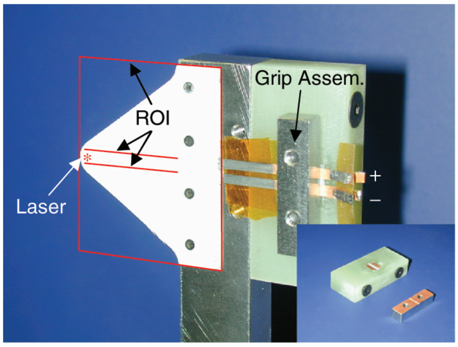

Fig. 8 Close-up of the chevron specimen mounted on a post.

B. Numerical Modeling

A thermoelastic model for SMA and SMAHC materials was previously implemented in the commercial finite element (FE) codes MSC.Nastran and ABAQUS. The model assumes that the SMA material is in a 1-D actuator form (i.e., wire or ribbon) consolidated within or between layers of a composite matrix and that the actuation authority is driven by application of a thermal load. The model is based upon definition of an effective (nonlinear) coefficient of thermal expansion (CTE) to represent the transformation and thermal strain of the SMA material in the actuation direction:

$$\sigma_{1a}(T) = E_a(T)\left[\varepsilon_1 - \int_{T_0}^{T} \alpha_{1a}(\tau)\,\mathrm{d}\tau\right] \tag{1}$$

It can be shown that the thermal strain in Eq. (1) is governed by thermoelasticity at temperatures below A_s and is related to the recovery stress $\sigma_r(T)$ and modulus at higher temperatures ($T \geq A_s$):

$$\sigma_r(T) = -E_a(T)\int_{T_0}^{T}\alpha_{1a}(\tau)\,\mathrm{d}\tau \quad \text{or} \quad \int_{T_0}^{T}\alpha_{1a}(\tau)\,\mathrm{d}\tau = -\frac{\sigma_r(T)}{E_a(T)} \tag{2}$$

An expression analogous to Eq. (1) can be written for the actuator in the transverse direction:

$$\sigma_{2a}(T) = E_a(T)\left[\varepsilon_2 - \int_{T_0}^{T}\alpha_{2a}(\tau)\,\mathrm{d}\tau\right] \tag{3}$$

where it was assumed that Young's modulus for the SMA is directionally independent and $\alpha_{2a}(T)$ is not related to recovery stress but is still nonlinear due to differing martensitic and austenitic properties. Analogous expressions can be written for the composite matrix material:

$$\begin{gathered}\sigma_{1m}(T) = E_{1m}(T)\left[\varepsilon_1 - \int_{T_0}^{T}\alpha_{1m}(\tau)\,\mathrm{d}\tau\right] \quad \text{and}\\ \sigma_{2m}(T) = E_{2m}(T)\left[\varepsilon_2 - \int_{T_0}^{T}\alpha_{2m}(\tau)\,\mathrm{d}\tau\right]\end{gathered} \tag{4}$$

The expressions in Eqs. (1), (3), and (4) allow the SMA and matrix materials to be modeled as independent orthotropic layers or as SMAHC orthotropic layers. The latter case requires effective orthotropic properties for the mixture. It can be shown that one form for the effective properties of a SMAHC lamina can be constructed from the constituent relations as follows:

$$\begin{gathered}E_1 = E_a v_a + E_{1m} v_m \qquad E_2 = \frac{E_a E_{2m}}{E_a v_m + E_{2m} v_a}\\ \nu_{12} = \nu_a v_a + \nu_{12m} v_m \qquad G_{12} = \frac{G_a G_{12m}}{G_a v_m + G_{12m} v_a}\\ \int_{T_o}^{T}\alpha_1(\tau)\,\mathrm{d}\tau = \frac{E_a v_a \int_{T_o}^{T}\alpha_{1a}(\tau)\,\mathrm{d}\tau + E_{1m} v_m \int_{T_o}^{T}\alpha_{1m}(\tau)\,\mathrm{d}\tau}{E_a v_a + E_{1m} v_m}\\ \int_{T_o}^{T}\alpha_2(\tau)\mathrm{d}\tau = \int_{T_o}^{T}[\alpha_{2a}(\tau)v_a + \alpha_{2m}(\tau)v_m]\mathrm{d}\tau\end{gathered} \tag{5}$$

In either case, the preceding expressions form the basis for orthotropic constitutive relations for individual layers, and classical lamination theory can be used to develop the governing relations for a SMAHC laminate. Additional detail about the constitutive model can be found in [27]. Detail on the implementation in the commercial codes, procedures for using the constitutive model, and examples of analysis input files can be found in [28,29].

The constitutive model can be calibrated for a particular material system by data from appropriate measurements of the engineering properties in Eqs. (5). For example, the behavior of an actuator under stiff constraint and restricted to small prestrain recovery in service (e.g., the SMAHC chevron application) is well represented by measurements of the *blocked* (fixed-constraint) recovery stress. Concurrent knowledge of the modulus $E_a(T)$ then quantifies the axial effective thermal strain through Eq. (2). The remaining orthotropic properties for the SMA actuator material can be specified by using published values for Poisson's ratio, assuming Young's modulus and Poisson's ratio to be directionally independent, and assuming that the shear modulus can be related to the other properties through the isotropic relation $G_a = E_a/2(1 + \nu_a)$. Orthotropic material properties for typical composite matrix materials are easily determined by standard test techniques.

Thermomechanical characterization tests were previously performed on the nitinol ribbon material used in this study. Properties specific to the glass-epoxy matrix material used in this study were not available, and so approximate properties from a similar material system were used in the numerical predictions of the chevron performance. The temperature-dependent orthotropic properties that were used in this study to model the nitinol and glass-epoxy materials are shown in Table 1. The 2-direction CTE for nitinol $\alpha_{2a}(T)$ was interpolated between the A_s and A_f temperatures noted from the variation in Young's modulus $E_a(T)$, approximately 45 and 85°C, to model the variation within the austenitic transformation temperature range $A_s \to A_f$. Note that this A_f is greater than that measured by DSC because stress inhibits completion of the transformation. Additional detail on these topics can be found in [23,24] and will be discussed further subsequently.

A FE model of the adaptive SMAHC chevron was developed in MSC.Patran for pre- and postprocessing. The chevron geometry was meshed using 2000 quadrilateral (type CQUAD4/S4 in

Table 1 Orthotropic material properties for glass epoxy and nitinol, secant CTE data presented with $T_{\mathrm{ref}} = 21$°C

	Glass epoxy						Nitinol				
T, °C	α_{1m}, /°C	α_{2m}, /°C	E_{1m}, GPa	E_{2m}, GPa	G_{12m}, GPa	ν_{12m}	α_{1a}, /°C	α_{2a}, /°C	E_a, GPa	G_a, GPa	ν_a
15.6	5.22E − 06	1.08E − 05	49.299	19.996	9.653	0.29	6.61E − 06	6.61E − 06	27.166	10.449	0.3
21.1	0.00E + 00	0.00E + 00	49.299	19.996	9.653	0.29	6.61E − 06	6.61E − 06	27.166	10.449	0.3
26.7	5.53E − 06	1.23E − 05	49.299	19.996	9.653	0.29	6.61E − 06	6.61E − 06	24.799	9.538	0.3
32.2	5.81E − 06	1.40E − 05	49.230	19.720	9.446	0.29	−8.54E − 06	6.61E − 06	22.432	8.628	0.3
37.8	6.10E − 06	1.57E − 05	49.161	19.444	9.239	0.29	−2.16E − 05	6.61E − 06	20.064	7.717	0.3
43.3	6.30E − 06	1.71E − 05	49.092	19.203	9.067	0.29	−2.83E − 05	6.61E − 06	25.705	9.886	0.3
48.9	6.49E − 06	1.85E − 05	49.023	18.961	8.895	0.29	−3.67E − 05	6.61E − 06	31.345	12.056	0.3
54.4	6.58E − 06	1.93E − 05	48.920	18.720	8.722	0.29	−5.73E − 05	6.66E − 06	36.985	14.225	0.3
60.0	6.67E − 06	2.02E − 05	48.817	18.479	8.550	0.29	−8.16E − 05	6.79E − 06	42.625	16.394	0.3
65.6	6.70E − 06	2.07E − 05	48.748	18.203	8.412	0.29	−8.95E − 05	6.96E − 06	48.265	18.563	0.3
71.1	6.70E − 06	2.11E − 05	48.748	17.789	8.274	0.29	−8.77E − 05	7.16E − 06	54.857	21.099	0.3
76.7	6.68E − 06	2.13E − 05	48.713	17.410	8.102	0.29	−8.70E − 05	7.39E − 06	61.448	23.634	0.3
82.2	6.66E − 06	2.15E − 05	48.679	17.031	7.929	0.29	−8.71E − 05	7.63E − 06	64.206	24.694	0.3
87.8	6.63E − 06	2.16E − 05	48.644	16.617	7.757	0.29	−8.90E − 05	7.89E − 06	63.131	24.281	0.3
93.3	6.60E − 06	2.16E − 05	48.610	16.203	7.585	0.29	−8.97E − 05	8.13E − 06	62.055	23.867	0.3
98.9	6.59E − 06	2.16E − 05	48.610	15.755	7.171	0.29	−8.56E − 05	8.33E − 06	63.917	24.583	0.3
104.4	6.57E − 06	2.17E − 05	48.610	15.307	6.757	0.29	−8.21E − 05	8.51E − 06	65.778	25.299	0.3
110.0	6.57E − 06	2.17E − 05	48.575	14.859	6.378	0.29	−7.80E − 05	8.66E − 06	67.640	26.016	0.3
115.6	6.57E − 06	2.17E − 05	48.541	14.411	5.999	0.29	−7.33E − 05	8.80E − 06	69.502	26.731	0.3
121.1	6.58E − 06	2.18E − 05	48.541	13.997	5.585	0.29	−6.89E − 05	8.92E − 06	71.363	27.448	0.3
126.7	6.61E − 06	2.19E − 05	48.610	13.445	5.171	0.29	−6.69E − 05	9.03E − 06	70.839	27.246	0.3
132.2	6.64E − 06	2.20E − 05	48.644	12.928	4.723	0.29	−6.51E − 05	9.13E − 06	70.315	27.044	0.3
137.8	6.68E − 06	2.22E − 05	48.679	12.411	4.275	0.29	−6.33E − 05	9.22E − 06	69.791	26.843	0.3
143.3	6.71E − 06	2.23E − 05	48.748	11.894	3.861	0.29	−6.15E − 05	9.30E − 06	69.267	26.641	0.3
148.9	6.75E − 06	2.25E − 05	48.817	11.377	3.448	0.29	−5.96E − 05	9.37E − 06	68.743	26.440	0.3

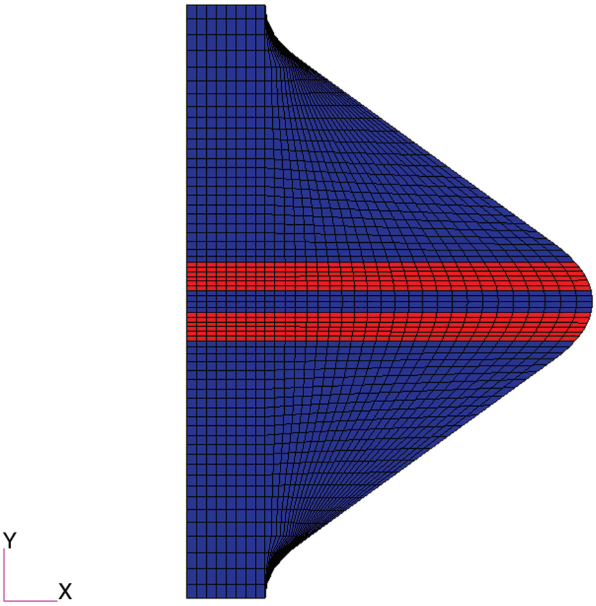

Fig. 9 SMAHC chevron geometry and FE mesh.

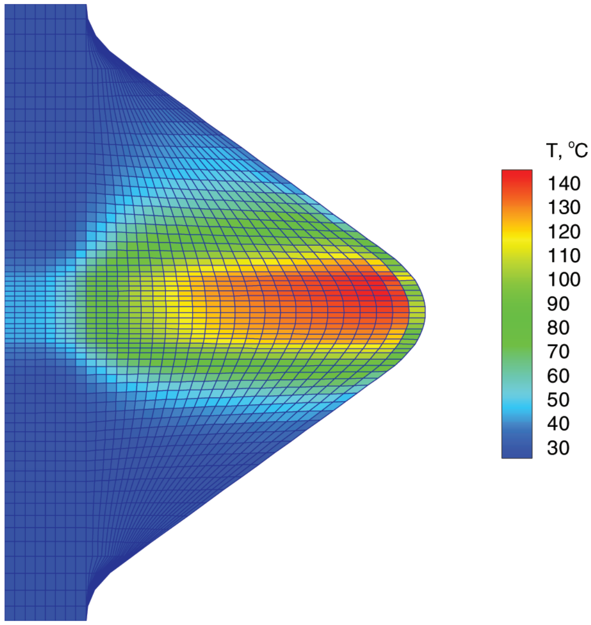

Fig. 10 Measured temperature distribution interpolated onto FE mesh.

MSC.Nastran/ABAQUS) and 48 triangular (type CTRIA3/S3 in MSC.Nastran/ABAQUS) shell elements, as shown in Fig. 9. The mesh was spatially converged and was constructed such that the width of each nitinol actuator assembly constituted four element widths. Thus, the red elements were composed of two layers of nitinol in addition to the five layers of glass epoxy $(-45/45/90/\mathrm{SMA}/45/\mathrm{SMA}/-45)$, and the blue elements had a lamination of glass-epoxy layers only $(-45/45/90/45/-45)$. The nitinol layers in the SMAHC elements had an orientation angle of 0 deg. Recall that the glass-epoxy plies surrounding the nitinol ribbon exhibited significant compaction during cure. The layer thickness distribution was modeled by dividing the measured thickness in the region away from the nitinol evenly between the 5 glass-epoxy layers, or 0.0127 cm per layer. The thickness of the nitinol layers was taken to be unchanged at 0.0152 cm per layer, and the balance of the thickness in the nitinol region was distributed evenly among the 5 glass-epoxy layers, or 0.0081 cm per layer.

The boundary conditions in the bench-top test configuration were modeled as follows. All 6 degrees of freedom were constrained at the screw-attachment nodal locations and at the base of the nitinol strips at the edge of the chevron. The out-of-plane translational 6 degrees of freedom were constrained over the entire mounting surface. The measured full-field temperature distribution at room temperature and at the three elevated temperature set points of 54, 88, and 121°C were interpolated onto the finite element nodal locations, as illustrated for the 121°C set point in Fig. 10, and used as the initial and load temperature distributions in the analysis. Nonlinear static analyses were performed in MSC.Nastran and ABAQUS (i.e., Solution 106 and ABAQUS/Standard, respectively), with the increment-dependent thermal load defined by interpolation between the measured temperature distributions. Ten uniform load increments were used between each measured temperature distribution. An iteration convergence criterion of 0.001 and 0.005 for residual force was specified for the MSC.Nastran and ABAQUS solutions, respectively.

C. Experimental and Numerical Results

The chevron was subjected to a total of 56 thermal cycles (tests) on the bench top. The maximum power consumption of the chevron in the course of these tests was nominally 3.5 W (1.6 V, 2.25 A) at the peak set-point temperature of 121°C. The deflection at the LDT spot location (denoted as *near tip*) versus set-point temperature (average centerline temperature of the top actuator assembly) for the 1st and 56th thermal cycles is shown in Fig. 11. Note that the chevron did not completely return to its original undeflected shape subsequent to the first thermal cycle, thereby leaving a slight curvature in the chevron and approximately 0.025 cm of near-tip deflection. The amount of additional *permanent deformation* decreased rapidly with thermal cycle and became relatively insignificant beyond thermal cycle 4. The permanent deformation resulted from the host structure not developing adequate restoring force (due to strain energy) during bending to fully reelongate the actuators upon retraction. The deficit in restoring force was primarily due to creep and microcracking in the composite matrix material. Another factor was the martensitic transformation associated with the nitinol. It is known that M_f for the actuator material used in this study is above room temperature under fixed-constraint conditions. However, the compliance offered by deformation of the composite structure relieved some stress, thereby lowering the M_f slightly and leaving the opportunity for less than full transformation to martensite.

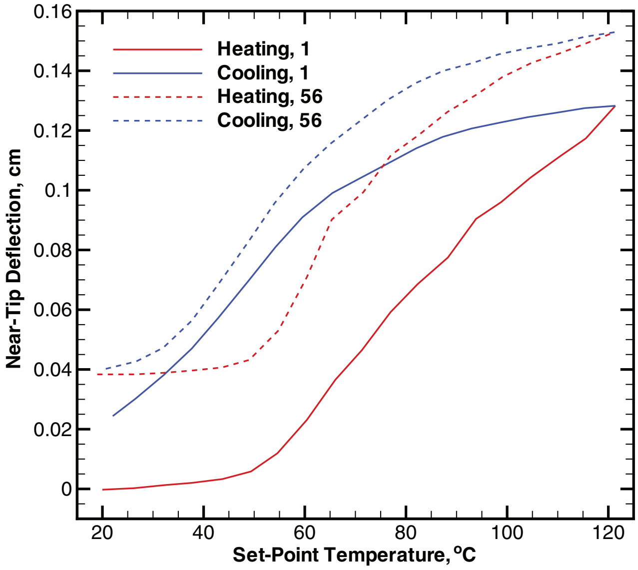

Fig. 11 Near-tip deflection vs set-point temperature for the 1st and 56th thermal cycles.

The nitinol actuators were not *trained* before fabrication, and so reductions in actuation authority and hysteresis were expected as the actuators were cycled. These reductions are known to accumulate quickly in the first several cycles and to stabilize after approximately 50 cycles for the nitinol material used in this study [23,24]. A decrease in hysteresis is evident in Fig. 11, but the near-tip deflection increased with cycle number despite the decrement in actuation authority. The growth of the maximum deflection with increasing cycle number was attributable to the combined effects of the permanent deformation and hysteresis in the actuator recovery stress. The effects of hysteresis are not obvious in Fig. 11 but were important and were realized during instances when the thermal controller overshot intermediate set-point temperatures during heating. The hysteresis effect was manifested by approximately constant actuator force/deflection during cooling to an intermediate set point after an overshoot event (as opposed to diminishing force/deflection during cooling), which resulted in an upward shift in the actuator force and structural deflection as the controller proceeded to heat to the next set point. It is clear that this effect can accumulate quickly with repeated set-point overshoot events. The actuator evolution and the permanent deformation effects stabilized by thermal cycle 50, leaving the chevron performance very repeatable, with avoidance of additional set-point overshoot events. The stabilized permanent (unactuated) and maximum (actuated) near-tip deflections, relative to the undeflected shape, were approximately 0.038 and 0.152 cm, respectively. The permanent deformation has implications for tests under representative flow conditions, as will be described in the next section.

The measured and predicted near-tip deflection versus set-point temperature for test 1 is shown in Fig. 12. Comparison with numerical prediction is only shown for the first test because the preceding permanent deformation for subsequent tests has a significant influence on the deflection response, and initial imperfections were not considered in the numerical model. It can be seen that the agreement between the measurements and predictions is excellent, with the predictions from MSC.Nastran and ABAQUS being practically indistinguishable. The quality of the agreement between the LDT and PMI measurements is typical of all of the tests. The observed differences are attributable to uncertainty in the longitudinal placement of the two measurements because of the large rotation (slope) near the chevron tip. Specifically, the LDT and PMI measurement locations move toward the tip as the chevron deflection increases, because rotation moves the chevron tip in the negative x direction while deflecting in the z direction. This effect leads to a small systematic error in the measured deflections manifested as slightly deteriorating agreement with the numerical model as the deflection increases. Corresponding results comparing measured and predicted centerline deflection profiles versus set-point temperature for test 1 are shown in Fig. 13. The centerline profile is shown at ambient temperature and at three elevated temperatures: 54, 88, and 121°C. It can be seen that the predicted and measured results are in excellent agreement in both deflection amplitude and shape. Note that the PMI deflection data were fit to remove variability due to surface roughness.

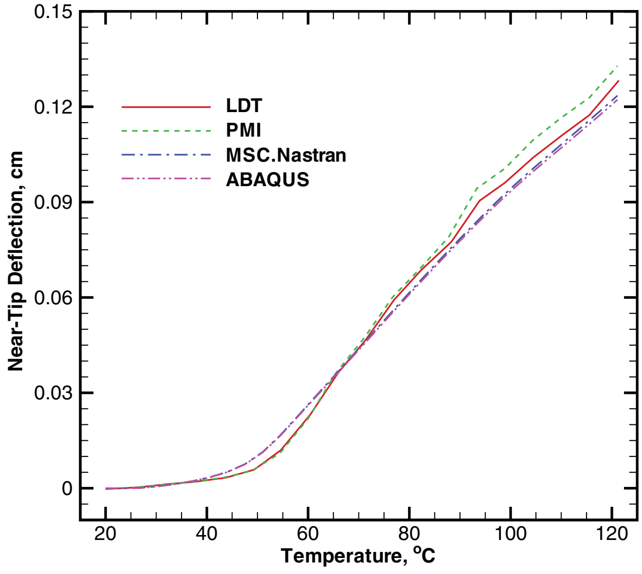

Fig. 12 Measured and predicted deflection vs temperature for test 1.

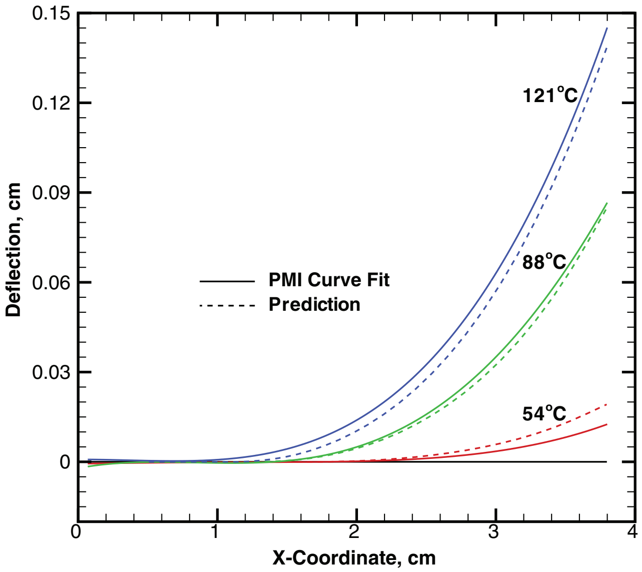

Fig. 13 Measured and predicted centerline deflections at four temperatures for test 1.

IV. Testing with Representative Flow Conditions

The chevron was tested further in the NASA LaRC Small Anechoic Jet Facility (SAJF) to explore nozzle integration issues and to examine the effects of representative flow conditions on the chevron temperature distribution, power consumption, deflection performance, and deflection controllability.

A. Experimental Arrangement

The test apparatus consisted of the SAJF apparatus, the chevron/nozzle assembly, the IR and PMI systems, the LDT, and a control and data acquisition system interfaced with the chevron instrumentation and a dc power supply. A schematic of the overall SAJF test configuration is shown in Fig. 14. The SAJF apparatus consisted of a heated and pressurized air-supply system providing controlled flow conditions to a nozzle assembly, which entrains flow about the supply duct and exhausts into a semi-anechoic test cell. A flow collector and exhaust fan maintained nominally ambient temperature and pressure conditions in the test cell. The PMI and IR systems were configured on an optical bench within the test cell at a distance of approximately 61 cm from the chevron. Upon actuation, the chevron

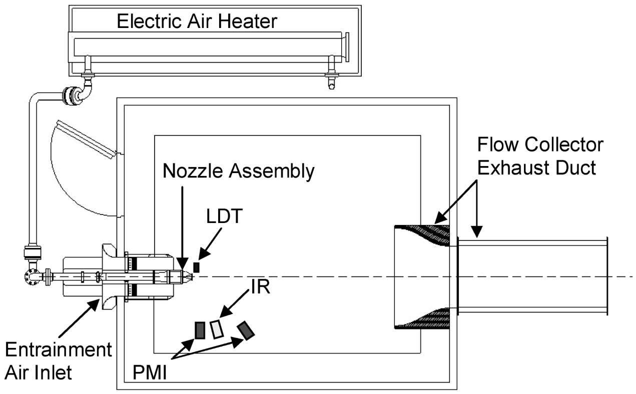

Fig. 14 Top-view schematic of the SAJF test configuration.

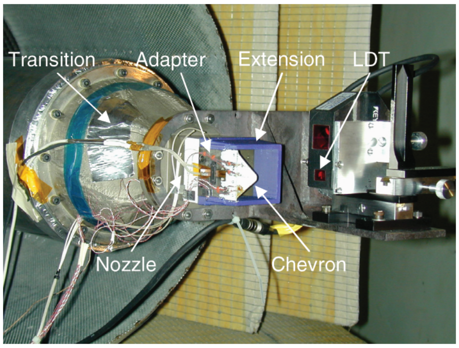

Fig. 15 **Detail of chevron-adapter assembly, nozzle, and transition to the supply duct.**

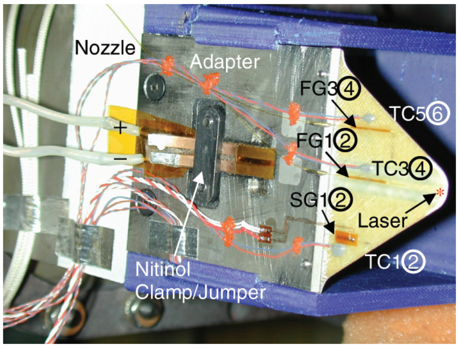

Fig. 16 **Detail of chevron instrumentation and power connectivity.**

deflected away from the IR and PMI systems and into the flow. The LDT was mounted to a bracket attached to the nozzle assembly.

Details of the chevron and nozzle assembly are shown in Fig. 15. Progressing in the flow direction, from left to right in the photograph, the nozzle assembly consisted of a round (15.24-cm diameter) to square transition piece and a 5.08×5.08 cm square nozzle. The chevron and stainless steel adapter assembly was mounted to the square nozzle. A three-sided nozzle extension provided the other three sides of flow containment over the length of the stainless steel adapter. A close-up of the chevron-adapter assembly is shown in Fig. 16. Note that this picture was taken before painting this surface of the chevron white for the PMI measurements. All of the nitinol was configured electrically in series in a manner similar to that achieved in the bench-top tests. The red asterisk in Fig. 16 indicates the location of the LDT spot on the flow side of the chevron and approximately 0.140 cm from the tip.

The chevron was instrumented with three pairs of back-to-back strain transducers: that is, transducer pairs mounted at the same planform location but on opposite sides of the chevron. One pair of fiber optic strain gauges was attached at the chevron centerline, indicated in Fig. 16 by FG1 and FG2. Another pair of fiber gauges (FG3 and FG4) was attached at the upper outboard location. The fiber gauges used a single light source and their output was multiplexed. The fiber gauges were employed to help discern the trends in the strain response because of their low-temperature sensitivity. A pair of conventional (foil) gauges was mounted at the lower outboard location, indicated by SG1 and SG2, and each gauge constituted the single active arm of a separate quarter-bridge. All strain transducers measured the longitudinal (flow direction) normal strain. A 36 American Wire Gauge type-T thermocouple was mounted in the vicinity of and at the midspan of the gauge length of each strain transducer, as indicated in Fig. 16 by TC1–TC6. The circled numbers in Fig. 16 indicate transducers on the flow side of the chevron. Flow-side thermocouples were located on the opposite side of the corresponding strain transducers than the thermocouples visible on the side opposite the flow in Fig. 16 (e.g., TC2 was above SG2).

Electrical power was supplied to the chevron by a dc power supply operated in constant current mode and commanded by analog voltage from a control system that took input from the strain, thermocouple, and LDT instrumentation. Heating of the nitinol actuators was done in either an open-loop or closed-loop mode. In open-loop mode, a specified current level was applied to the actuators. In closed-loop mode, a proportional–integral controller with antiwindup (see Cabell et al. [30]) was used to regulate the current applied to the actuators to drive the chevron to a specified tip immersion. The output of the LDT was used for the feedback measurement in closed-loop mode.

B. Experimental Results

Initial tests were performed with the chevron without the effects of flow to investigate strain measurements from the fiber gauges in comparison with the foil gauges on the present and previous similar chevrons. The output of the fiber gauges on the centerline of the present chevron was consistent with expectation and free of the errors introduced by thermal sensitivity of foil gauges placed at the same locations on previous chevrons. The strain responses measured by the outboard fiber and foil transducer pairs on the present chevron were qualitatively similar. Thus, it was concluded that the strain field is most complex in the vicinity of the embedded actuators, as expected, and the strain field in the outboard regions is better for control purposes. Additional insight into these observations will be given later in this section.

Recall that this study is focused on simulated bypass flow conditions because of the temperature limitations of commercially available SMAs ($A_s \leq 110^\circ\mathrm{C}$ for nitinol). The test conditions shown in Table 2 were established as representative of the bypass flow environment of desirable engine configurations (i.e., bypass ratios 5 and 8) at takeoff and climb conditions. Terms in the table include nozzle pressure ratio (NPR), total temperature T_t, total pressure P_t, Mach number/temperature/velocity according to ideal-gas relations $M_{\mathrm{ideal}}/T_{\mathrm{ideal}}/V_{\mathrm{ideal}}$, and the adiabatic-wall temperature T_{aw}, assuming turbulent flow conditions. Other quantities needed to produce the tabulated quantities are the ideal-gas constant $287\ \mathrm{m}^2/(\mathrm{s}^2 \cdot \mathrm{K})$, specific heat ratio of 1.4, flow area of $25.8\ \mathrm{cm}^2$, and ambient pressure of 101.36 kPa. Although flow at a higher total temperature (e.g., of 82°C) is more representative of actual bypass-nozzle flow conditions, flow at a total temperature of 27°C is the focus of this study because heat transfer between the flow and the chevron is governed by T_{aw} and the A_s temperature for the nitinol alloy is 45°C. Thus, the 27°C flow enables the entire chevron actuation authority to be effected by control stimulus, and the low-temperature flow is expected to have negligible effect on jet noise simulation.

A typical test in the SAJF consisted of the following. A run without flow was performed first in each case to serve as a baseline. Then flow was established at a constant total temperature, and pressure was controlled to successively achieve each of the NPR settings in Table 2 in either ascending or descending order. Open- and/or

Table 2 **Flow parameters associated with the tests performed on the chevron in the SAJF**

Test point	NPR	T_t, °C	M_{ideal}	P_t, kPa	T_{ideal}, °C	V_{ideal}, m/s	Flow, kg/s	T_{aw}, °C	Comments[a]
1	1.46	27	0.756	147.98	−4.1	248.5	0.841	23.3	BPR 8, CB
2	1.62	27	0.860	164.20	−11.9	278.6	0.972	22.4	BPR 8, TO
3	1.75	27	0.931	177.37	−17.6	298.4	1.064	21.8	BPR 5, TO

[a] BPR denotes the bypass ratio, TO denotes takeoff, and CB denotes climb.

closed-loop chevron runs were conducted with constant NPR at each of the settings in a test. Performance data associated with each of the chevron runs included the LDT, strain, thermocouple, and IR thermography data collected throughout the run and PMI data (50-frame averages) were collected at specific conditions of interest within the run. Initial tests were focused on establishing repeatability and investigating essential parameters such as the current (power) required to bring the top actuator-assembly centerline average temperature to nominally 121°C, as indicated by IR measurements. The nominal current (power) required to achieve the 121°C set point at NPRs of 1.46, 1.62, and 1.75 was 7.35 (42.5), 7.75 (47.2), 8.125 (51.9) A (W), respectively.

1. Open-Loop Results

Representative near-tip deflection results from open-loop runs without flow and with flow at the three NPRs are shown in Fig. 17. Recall that the chevron was permanently deformed after the bench-top testing. This deformed state was considered to be the new *reference* or zero-deflection state for the SAJF tests described here. The chevron was nominally in the new reference state at the start of testing and after the initial tests to compare strain responses from the two gauge types, as indicated by the near-tip deflection of -0.005 cm at time $t = 0$ in Fig. 17. The first 12 min of data in Fig. 17 correspond to the no-flow condition and show a chevron near-tip *relative* immersion, heated minus unheated near-tip position, of 0.145 cm as the nitinol was heated by 2.25 A of current. The slow thermal response of the chevron is evident in this no-flow case, in which heating and cooling occurred over several minutes. Note that the maximum deflection for this no-flow run exceeded that for the bench-top tests. This enhanced performance was attributable to the fact that the chevron was driven to a higher temperature: namely, a control temperature of 132°C instead of 121°C.

Flow was initiated at $\sim t = 12$ min and the NPR setting of 1.75 was achieved at $\sim t = 20$ min. The negative deflection (retraction) values indicate that the chevron was deflected away from the flow (and the new reference shape) and toward the original undeflected (flat) shape as the NPR increased. The flow-induced relative retraction was 0.038 cm. The open-loop controlled performance shows rapid heating and relative immersion of 0.102 cm followed by rapid cooling and retraction. The NPR was decreased to 1.62 from $\sim t = 27$ to 30 min and the reduced pressure allowed the chevron to recover 0.005 cm of the permanent deflection. The open-loop run at the 1.62 NPR produced a relative immersion of 0.109 cm. The pressure was reduced again at $\sim t = 36$ min and achieved the 1.46 NPR at $\sim t = 39$ min. The chevron recovered an additional 0.008 cm of the permanent deflection at the reduced pressure and an open-loop run at $\sim t = 40$ min produced a relative immersion of 0.117 cm. The deflection response of the chevron in all of the runs with flow was quite rapid because of the ability to readily dissipate heat, which will be illustrated subsequently.

The actuation-induced relative immersion and flow-induced relative retraction were repeatable within tests and between tests to approximately ±0.003 cm. Consequently, the deflection relative to the permanently deflected reference state (the absolute deflection), due to actuation and/or flow, was also very repeatable with similar accuracy. The average relative near-tip immersion values due to actuation at the 121°C set point were 0.119 cm without flow and 0.117, 0.109, 0.102 cm with flow at NPRs of 1.46, 1.62, and 1.75, respectively. The average relative near-tip retraction values due to flow without actuation were 0.023, 0.030, and 0.038 cm for the three NPRs, respectively. It is clear that the immersion control (actuation authority) is relatively insensitive to the flow loading, and the flow assisted in returning the chevron toward the original undeflected shape in the unactuated condition, nominally returning to the original undeflected shape at the highest NPR of 1.75. The most notable variation in the testing was the chevron near-tip position at the beginning of each test, which depended on the conditions at the end of the previous test (e.g., flow versus no flow). It was found that this effect could always be rectified by subjecting the chevron to a thermal cycle without flow to regain the permanently deflected reference configuration.

The strain response from the open-loop runs, corresponding to the deflection response in Fig. 17, is shown in Fig. 18. The flow-side strain transducers showed greater strain level and range than their counterparts on the freestream side in all cases and at all conditions. This difference is attributable to the fact that the contractile (negative) in-plane strain is subtractive from the positive bending strain on the freestream side, but it is additive with the negative bending strain on the flow side. The strain response of gauge pairs SG1-SG2 and FG3-FG4 were qualitatively similar with flow, consistent with notes at the beginning of this subsection for the initial tests without flow, but were significantly different quantitatively at all test conditions. This difference is due to the fact that, although the two gauge pairs were located symmetrically about the chevron centerline, their positions were different in the flow-wise direction. Also, the strain field in the chevron is asymmetric due to slight bend-twist coupling that arises from the stacking sequence. Both of these factors are shown in the plots of the nonlinear strain field on the flow and freestream sides of the chevron in Figs. 19 and 20, respectively. The strain contours were generated in ABAQUS and represent the x-direction logarithmic strain corresponding to the 121°C set point without aerodynamic load, and so they nominally correspond to the peak strains in the no-flow segment of Fig. 18. It can be seen that the

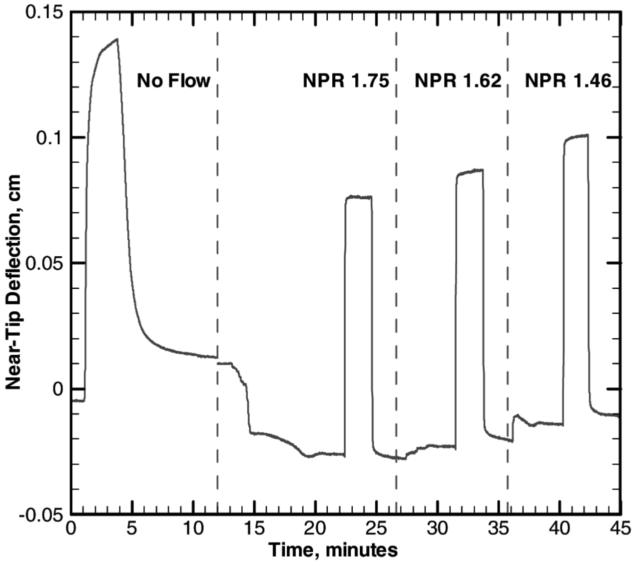

Fig. 17 Near-tip deflection in open-loop runs without flow and at the three NPR settings.

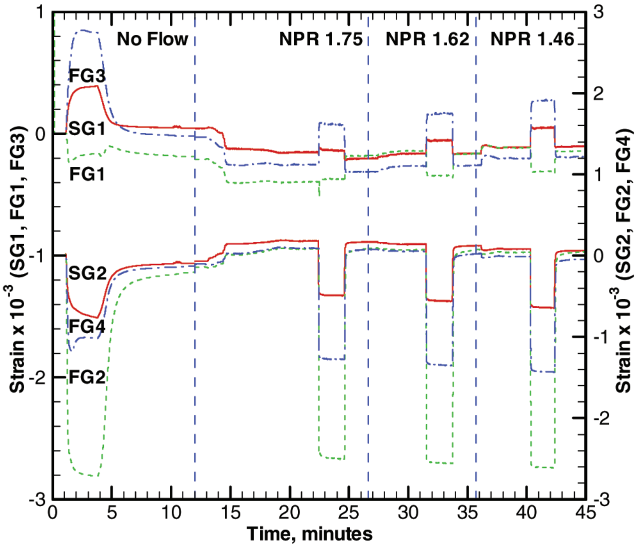

Fig. 18 Strain in open-loop runs without flow and at the three NPR settings.

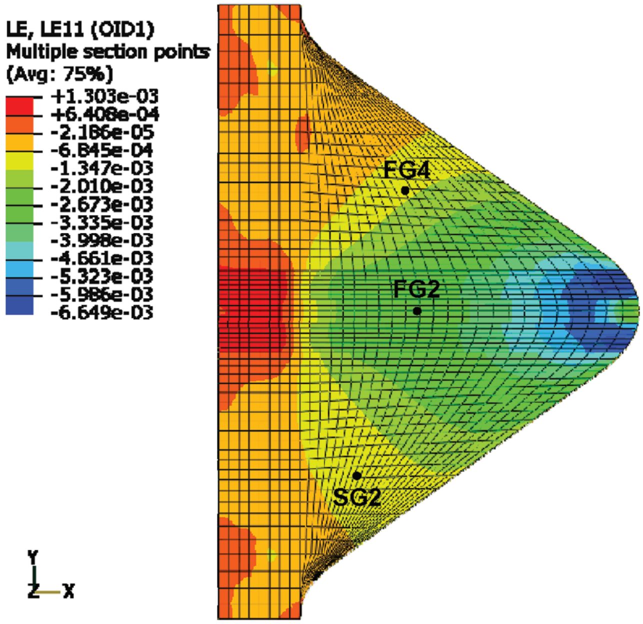

Fig. 19 Computed strain contours on the flow side at the 121°C set point without flow.

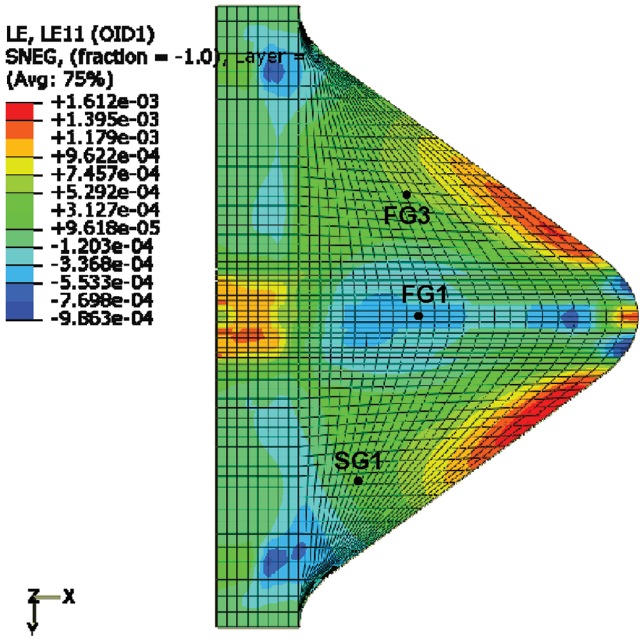

Fig. 20 Computed strain contours on the freestream side at the 121°C set point without flow.

computed strain contours compare well with the measured peak strains.

The thermocouple results for the same open-loop runs are shown in Fig. 21. It can be seen that heating was significant at all locations in the runs without flow (e.g., the first 12 min of data in Fig. 21), which was consistent with the bench-top testing. Heating in the vicinity of the foil gauges (i.e., TC1 and TC2) was least significant because they were spaced well below the actuators so that they benefited significantly from free-convection effects. Temperature differences within pairs of thermocouples were attributable to differences in proximity to the heat source and free-convection effects. Rapid thermal response was achieved in the runs with flow because of the direct heating and effective forced-convection cooling. The chevron control temperature was well represented by TC3 measurements, as illustrated by the peak temperatures in the runs with flow.

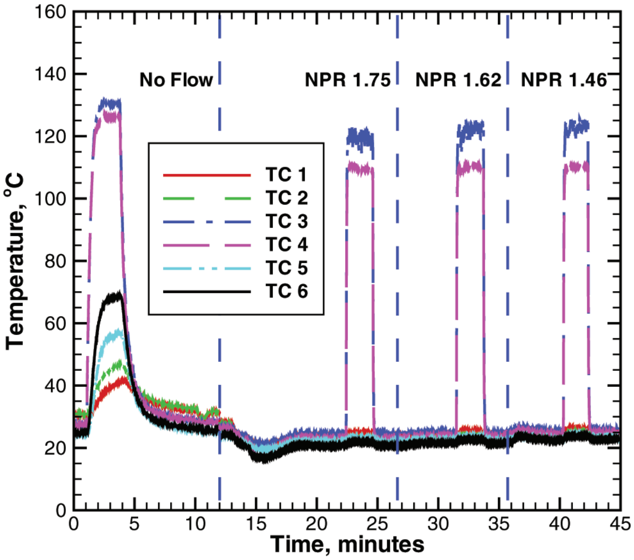

Fig. 21 Temperatures in open-loop runs without flow and at the three NPR settings.

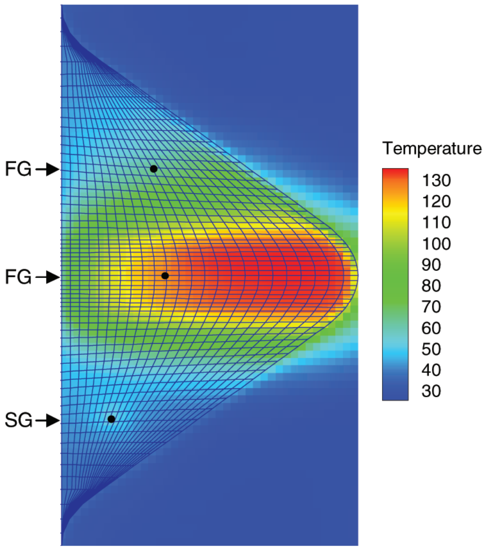

Fig. 22 Temperature distribution at 121°C set point with no flow.

Temperatures below that of the room were recorded at the outboard locations for the duration of the runs with flow and at the TC2 and TC3 locations during times of no heat addition, because T_{aw} was slightly less than room temperature. Flow-side temperatures were always coolest in each thermocouple pair because the subambient T_{aw} governed the dominant forced-convection mode of heat transfer. These observations are substantiated by the temperature fields measured by the IR camera at the 121°C set point without and with flow at the 1.75 NPR in Figs. 22 and 23, respectively. Thus, it can be concluded that the foil gauge results in this study suffered only minor temperature effects (apparent strain) for cases not involving flow and negligible effects for cases with flow. Furthermore, temperature effects are not a concern for any foil gauge location away from the actuators as long as the T_{aw} of the flow is near room temperature.

2. *Closed-Loop Results*

The chevron was assumed to behave like a first-order system for development of the controller. Step-response data were collected from the chevron with flow and were used to specify the parameters of the first-order model. Then proportional and integral gains of the controller were manually adjusted offline to achieve rapid response for disturbance rejection without overshoot or excessive current. Additional detail about the controller can be found in [30].

Representative closed-loop results for a run with flow at the 1.75 NPR setting are shown in Figs. 24–26. The output of the LDT was used for feedback. The closed-loop run was started after an open-loop run at the same NPR, for which the final near-tip deflection was −0.030 cm. Near-tip positions of 0.038, 0.058, and 0.000 cm were commanded as shown with the corresponding chevron response in Fig. 24. It can be seen that excellent control performance was achieved while increasing (heating) and decreasing (cooling) the immersion. The filled circles at the beginning and end of the set-point distribution indicate the onset and termination of closed-loop control. The current commanded by the controller to achieve the prescribed near-tip position distribution is shown in Fig. 25. It can be seen that the rapid and overdamped deflection response was easily achieved with a maximum current input of approximately 6.8 A.

Least-squares regression analysis was performed on the measured data from the open-loop runs (i.e., the data in Figs. 18 and 21) to build statistical models for estimating the near-tip displacement response based upon subsets of the chevron transducers, with the full set consisting of all six strain gauges and all six thermocouples. Variability in model accuracy with data from subsets of the open-loop runs was also investigated: that is, models built with data from all NPR settings, from combinations of NPR settings, and from individual NPR settings. The relative merit of each model was judged by comparing the root-mean-square (rms) difference between the estimated and measured near-tip response for the closed-loop run at 1.75 NPR. Additional detail on this analysis and general comments from the results follow.

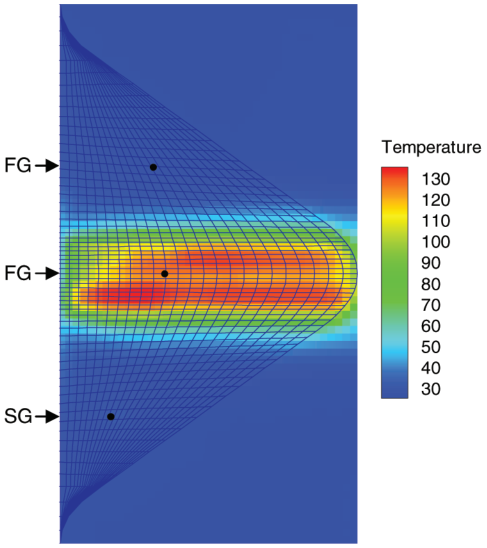

Fig. 23 Temperature distribution at 121°C set point with flow at 1.75 NPR.

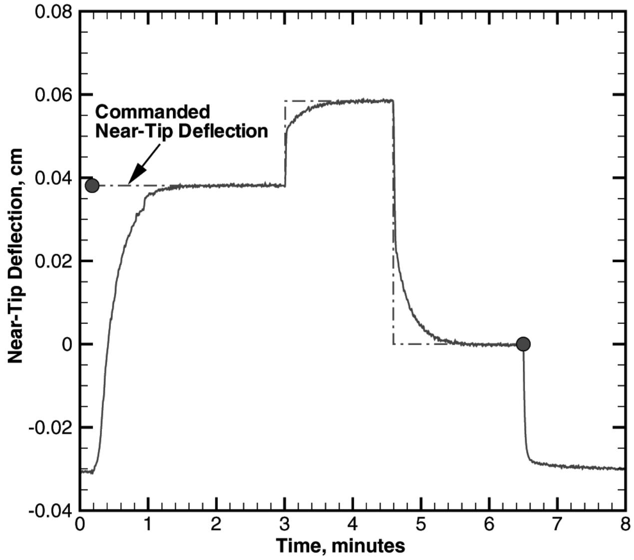

Fig. 24 Commanded and measured near-tip deflection with flow at a NPR of 1.75.

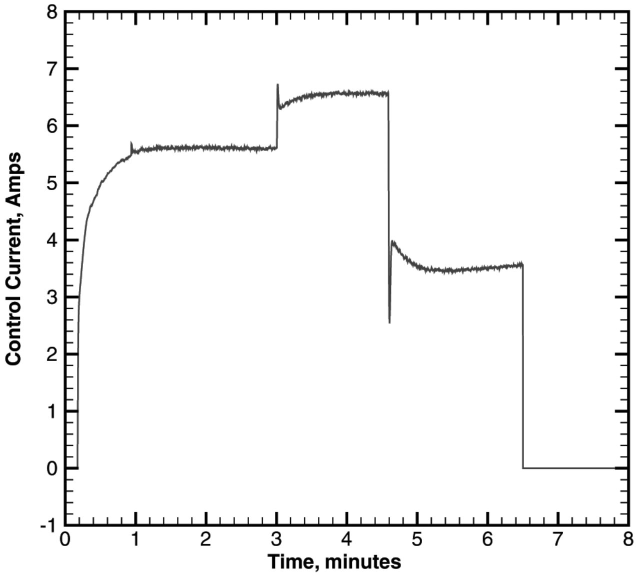

Fig. 25 Control current profile required to achieve the closed-loop response with flow at a NPR of 1.75.

An exhaustive search of all possible combinations of transducers, from 1 to all 12 transducers, was conducted to rank order the transducers in terms of rms prediction error on the closed-loop run. The search was conducted 7 times using all combinations of the open-loop data to build the regression models. For each combination of open-loop data, the prediction error decreased rapidly with inclusion of up to about 3 transducers in the model. The prediction error tended to plateau at a minimum value when using data from somewhere between 3 and 8 transducers and then increase with inclusion of transducers beyond 8. This behavior suggested that the models built with higher transducer counts were overfitting insignificant variations in the data set used to build the models that were not found in the data set against which the model was tested. The rank order of transducers varied with the number of transducers included in the model and with the subset of open-loop run data selected to build the model. SG2 was found to be the most important transducer in all cases. SG1, TC3, and TC4 were also very prominent. The fiber gauge data did not contribute to the model as well as would be expected because of time lag involved in the measurement system due to multiplexing of the optical channels. The thermocouple data at the outboard locations (i.e., TC1, TC2, TC5, and TC6) were also not particularly important because the temperature at those locations was dominated by the T_{aw} of the flow.

Models built exclusively with the 1.75 NPR open-loop run data exhibited the best accuracy and convergence rate with increasing transducer count. The best 3-transducer estimate was obtained using SG2, TC3, and TC4 from the 1.75 NPR open-loop run, which is shown in Fig. 26, and resulted in an rms error of 0.001 cm. This error is of the same order as the accuracy of the LDT measurement. Models from combinations of NPR settings including the 1.75 run performed reasonably well, but the accuracy and convergence rate suffered to an increasing extent with increasing data extraneous to the 1.75 NPR open-loop case. Models from combinations of open-loop run data that excluded the 1.75 NPR case performed rather poorly, as anticipated. It is hypothesized that availability of additional measurements that characterize the flow parameters (e.g., NPR and total temperature of the flow) would improve the model accuracy with inclusion of such extraneous build data. In any case, it is clear

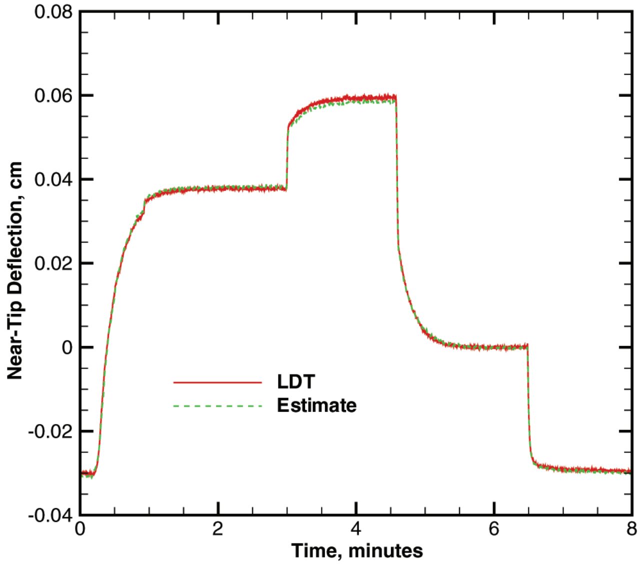

Fig. 26 Tip deflection estimate from strain and temperature measurements with flow at a NPR of 1.75.

that the best models are obtained from open-loop data that accurately capture the variation of the important parameters in ranges that closely span the anticipated closed-loop performance.

V. Conclusions

Static chevron systems are a proven noise-reduction technology for jet engines, but parametric effects of immersion amount and azimuthal distribution of immersion are not well understood. A novel means for interrogation of these parameters was developed in the present work via an adaptive-chevron concept. The concept involves embedding prestrained SMA actuators on one side of the neutral axis of the laminated-composite (termed a shape memory alloy hybrid composite) chevron to generate a thermal moment and deflect the structure out of plane when heated. The force developed in the host structure during deflection and the aerodynamic load due to the engine flow are used to restore the structure to the retracted position. An adaptive-chevron design was developed using a finite element model incorporating a commercially available constitutive model for shape memory alloy hybrid composite materials. The design and fabrication approach were very effective in terms of enabling minimal actuator content (weight), minimal structural thickness, and electrical heating of the SMA actuators. Very low variability between fabricated chevrons was also afforded.

The chevron was subjected to thermal cycles between ambient temperature and 121°C. Although the nitinol actuator force was known to diminish with thermal cycle, because the actuators were trained in situ, the maximum chevron tip deflection increased with thermal cycling. This effect was attributable to permanent deformation in the structure and hysteresis in the nitinol recovery stress that was brought on by overshoot in the thermal controller. The permanent structural deformation resulted from creep and microcracking in the composite matrix material. The permanent deformation could be reduced with less rotation of the angled plies in the lamination scheme, possibly at the expense of reduction in tip deflection. Controller overshoot (minor hysteresis excursions) should be avoided to produce consistent chevron performance. However, this effect could be exploited to increase the maximum tip deflection at the probable expense of increased permanent deformation. Excellent agreement was achieved between numerical predictions and experimental measurements in both deflection amplitude and 3-D shape. However, it was found that numerical models require a high degree of fidelity, including measured structural thickness distribution (and thickness-direction estimates of actuator locations) and measured thermal load, to compare well with experimental measurements of chevron performance.

Tests were also conducted on the chevron with flow representative of the bypass duct of a typical commercial engine at takeoff and climb conditions. Engine flow was effective at removing permanent deformation from the stabilized chevrons. The combination of electrical heating of the embedded actuators and forced convection from engine flow resulted in rapid chevron response. The strain response in the vicinity of the embedded actuators was complex and fraught with large temperature excursions. However, conventional foil strain gauges were sufficient for structural measurements when positioned at locations away from the actuators. The chevron relative immersion, powered position minus unpowered position, was found to be relatively insensitive to the nozzle pressure ratio over the range studied. All aspects of the chevron performance were very repeatable. Excellent closed-loop performance to prescribed tip positions was achieved. Excellent closed-loop performance was also demonstrated via a statistical model (least-squares regression) involving strain and temperature measurements, achieving a root-mean-square accuracy of approximately ±0.001 cm relative to a tip displacement measurement. Controller models should be developed from an open-loop performance database that closely spans the anticipated closed-loop operation range (i.e., does not include data from significant excursions outside of the expected operation range).

An adaptive-chevron concept was developed that meets the application requirements and is repeatable and controllable with typical performance measurements. A firm foundation was established upon which to extend this technology to chevrons with nozzle curvature. This paper also serves as a significant contribution to the infrastructure needed for development of adaptive-chevron nozzle assemblies.

Acknowledgments

The authors gratefully acknowledge the following contributors to this work: Sean Britton, George Hilton, Felecia Berry, John Swartzbaugh, Jeff Collins, Jeff Conover, and Clinton Reese (NASA Langley Research Center); Larry Becker and Brian Howerton (Lockheed Martin); and Mark Roth and Mark Clemons (Modern Machine and Tool Company).

References

[1] Saiyed, N. H., Mikkelsen, K. L., and Bridges, J. E., “Acoustics and Thrust of Separate-Flow Exhaust Nozzles with Mixing Devices for High-Bypass-Ratio Engines,” 6th AIAA/CEAS Aeroacoustics Conference, AIAA Paper 2000-1961, 2000.

[2] Thomas, R. H., Kinzie, K. W., and Pao, S. P., “Computational Analysis of a Pylon-Chevron Core Nozzle Interaction,” 7th AIAA/CEAS Aeroacoustics Conference, AIAA Paper 2001-2185, 2001.

[3] Callender, B., Gutmark, E., and Martens, S., “A Near-Field Investigation of Chevron Nozzle Mechanisms,” 9th AIAA/CEAS Aeroacoustics Conference and Exhibit, AIAA Paper 2003-3210, 2003.

[4] Massey, S. J., Thomas, R. H., Abdol-HAmid, K. S., and Elmiligui, A. A., “Computational and Experimental Flow Field Analyses of Separate Flow Chevron Nozzles and Pylon Interaction,” 9th AIAA/CEAS Aeroacoustics Conference and Exhibit, AIAA Paper 2003-3212, 2003.

[5] Rask, O., Gutmark, E., and Martens, S., “Acoustic Investigation of a High Bypass Ratio Separate Flow Exhaust System,” 42nd AIAA Aerosciences Meeting and Exhibit, AIAA Paper 2004-9, 2004.

[6] Koch, L. D., Bridges, J., and Khavaran, A., “Mean Flow and Noise Prediction for a Separate Flow Jet with Chevron Mixers,” 42nd AIAA Aerosciences Meeting and Exhibit, AIAA Paper 2004-189, 2004.

[7] Callender, B., Gutmark, E., and Martens, S., “A PIV Flow Field Investigation of Chevron Nozzle Mechanism,” 42nd AIAA Aerosciences Meeting and Exhibit, AIAA Paper 2004-191, 2004.

[8] Bridges, J., and Brown, C. A., “Parametric Testing on Chevrons on Single Flow Hot Jets,” 10th AIAA/CEAS Aeroacoustics Conference, AIAA Paper 2004-2824, 2004.

[9] Thomas, R. H., and Kinzie, K. W., “jet-Pylon Interaction of High Bypass Ratio Separate Flow Nozzle Configurations,” 10th AIAA/CEAS Aeroacoustics Conference, AIAA Paper 2004-2827, 2004.

[10] Doty, M. J., Henderson, B. S., and Kinzie, K. W., “Turbulent Flow Field Measurements of Separate Flow Round and Chevron Nozzles with Pylon Interaction Using Particle Image Velocimetry,” 10th AIAA/CEAS Aeroacoustics Conference, AIAA Paper 2004-2826, 2004.

[11] Callender, B., Gutmark, E., and Martens, S., "Far-Field Acoustic Investigation into Chevron Nozzle Mechanisms and Trends," *AIAA Journal*, Vol. 43, No. 1, 2005, pp. 87–95.
doi:10.2514/1.6150

[12] Mengle, V. G., "Relative Clocking of Enhanced Mixing Devices for Jet Noise Benefit," 43rd AIAA Aerospace Sciences Meeting and Exhibit, AIAA Paper 2005-996, 2005.

[13] Mengle, V. G., "Jet Noise Characteristics of Chevrons in Internally Mixed Nozzles," 11th AIAA/CEAS Aeroacoustics Conference, AIAA Paper 2005-2934, 2005.

[14] Massey, S. J., Elmiligui, A. A., Hunter, C. A., Thomas, R. H., and Pao, S. P., "Computational Analysis of a Chevron Nozzle Uniquely Tailored for Propulsion Airframe Aeroacoustics," *12th AIAA/CEAS Aeroacoustics Conference*, AIAA Paper 2006-2436, 2006.

[15] Mengle, V. G., Elkoby, R., Brusniak, L., and Thomas, R. H., "Reducing Propulsion Airframe Aeroacoustic Interactions with Uniquely Tailored Chevrons, 1: Isolated Nozzles," 12th AIAA/CEAS Aeroacoustics Conference, AIAA Paper 2006-2467, 2006.

[16] Bruck, H. A., Moore, C. L., and Valentine, T. L., "Repeatable Bending Actuation in Polyurethanes Using Opposing Embedded One-Way Shape Memory Alloy Wires," *Smart Materials and Structures*, Vol. 11, No. 4, 2002, pp. 509–518.
doi:10.1088/0964-1726/11/4/305

[17] Kim, C., Park, B.-S., and Goo, N.-S., "Shape Changes by Coupled Bending and Twisting of Shape-Memory-Alloy-Embedded Composite Beams," *Smart Materials and Structures*, Vol. 11, No. 4, 2002, pp. 519–526.
doi:10.1088/0964-1726/11/4/306

[18] Chandra, R., "Active Shape Control of Composite Blades Using Shape Memory Actuation," *Smart Materials and Structures*, Vol. 10, No. 5, 2001, pp. 1018–1024.
doi:10.1088/0964-1726/10/5/318

[19] Baz, A., Chen, T., and Ro, J., "Shape Control of Nitinol-Reinforced Composite Beams," *Composites, Part B*, Vol. 31, No. 8, 2000, pp. 631–642.
doi:10.1016/S1359-8368(00)00034-2

[20] Calkins, F. T., and Butler, G. W., "Subsonic Jet Noise Reduction Variable Geometry Chevron," 42nd AIAA Aerospace Sciences Meeting and Exhibit, AIAA Paper 2004-0190, 2004.

[21] Mabe, J. H., Cabell, R. H., and Butler, G. W., "Design and Control of a Morphing Chevron for Takeoff and Cruise Noise Reduction," 11th AIAA/CEAS Aeroacoustics Conference, AIAA Paper 2005-2889, 2005.

[22] Calkins, F. T., Butler, G. W., and Mabe, J. H., "Variable Geometry Chevrons for Jet Noise Reduction," 12th AIAA/CEAS Aeroacoustics Conference, AIAA Paper 2006-2546, 2006.

[23] Turner, T. L., "Thermomechanical Response of Shape Memory Alloy Hybrid Composites," NASA TM-2001-210656, 2001.

[24] Turner, T. L., Lach, C. L., and Cano, R. J., "Fabrication and Characterization of SMA Hybrid Composites," *Smart Structures and Materials 2001: Active Materials: Behavior and Mechanics*, edited by C. S. Lynch, Proceedings of SPIE, Vol. 4333, SPIE—The International Society for Optical Engineering, Bellingham, WA, 2001, pp. 343–354.

[25] Turner, T. L., "Structural Acoustic Response of a Shape Memory Alloy Hybrid Composite Panel (Lessons Learned)," *Smart Structures and Materials 2002: Smart Structures and Integrated Systems*, edited by L. P. Davis, Proceedings of SPIE, Vol. 4701, SPIE—The International Society for Optical Engineering, Bellingham, WA, 2002, pp. 592–603.

[26] Turner, T. L., Buehrle, R. D., Cano, R. J., and Fleming, G. A., "Modeling, Fabrication, and Testing of a SMA Hybrid Composite Jet Engine Chevron Concept," *Journal of Intelligent Material Systems and Structures*, Vol. 17, No. 6, June 2006, pp. 483–497.
doi:10.1177/1045389X06058795

[27] Turner, T. L., "A New Thermoelastic Model for Analysis of Shape Memory Alloy Hybrid Composites," *Journal of Intelligent Material Systems and Structures*, Vol. 11, No. 5, May 2000, pp. 382–394.
doi:10.1106/DTFJ-UFL3-XV0U-WJNA

[28] Turner, T. L., and Patel, H. D., "Input Files and Procedures for Analysis of SMA Hybrid Composite Beams in MSC.Nastran and ABAQUS," NASA TM-2005-213517, Jan. 2005.

[29] Turner, T. L., and Patel, H. D., "Analysis of SMA Hybrid Composite Structures in MSC.Nastran and ABAQUS," *Journal of Intelligent Material Systems and Structures*, Vol. 18, No. 5, May 2007, pp. 435–447.
doi:10.1177/1045389X06066699

[30] Cabell, R. H., Schiller, N. H., Mabe, J. H., Ruggeri, R. T., and Butler, G. W., "Feedback Control of a Morphing Chevron for Takeoff and Cruise Noise Reduction," *The 2004 International Symposium on Active Control of Sound and Vibration (ACTIVE 04)* [CD-ROM], Inst. of Noise Control Engineering, Iowa State Univ., Ames, IA, 2004, Paper a04-097.

J. Wei
Associate Editor